

pubs.acs.org/Macromolecules Article

# Ionic Effects on the Equilibrium Conformation of Catenated DNA Networks

Beatrice W. Soh, Ahmed Khorshid, Dana Al Sulaiman, and Patrick S. Doyle\*



Cite This: Macromolecules 2020, 53, 8502-8508



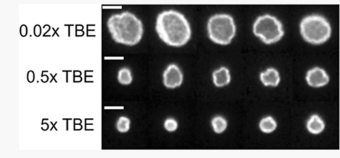
**ACCESS** 

Metrics & More

Article Recommendations

Supporting Information

**ABSTRACT:** In this work, we study the ionic effects on the equilibrium size and shape of kinetoplasts, a two-dimensional (2D) network of catenated DNA rings. With increasing ionic strength from 5 to 200 mM, we observe a decrease in kinetoplast size, primarily driven by the longrange electrostatic interactions that give rise to a change in effective DNA width. A fit of the experimentally measured kinetoplast size versus effective width yields a scaling exponent of 0.38. To probe the quantitative effects of ionic strength on kinetoplast size, we develop a scaling



argument based on a generalized Flory approach for a 2D polymer represented as monomers on an open lattice. Interestingly, while ionic strength has a significant effect on kinetoplast size, we find that it does not impact the kinetoplast shape.

## 1. INTRODUCTION

The study of how electrostatic interactions impact the conformations of polyelectrolytes in solution has long been a topic of interest in the scientific community. From the broadranging applications of polyelectrolytes<sup>1–3</sup> to the charged nature of many important biological macromolecules,<sup>4</sup> an understanding of the effect of electrostatic interactions on polyelectrolyte conformation is motivated by its widespread relevance. By changing the ionic conditions, one can tune the range of electrostatic interactions between charges on the polyelectrolytes and modulate the equilibrium conformation of the molecules.

For polyelectrolytes, electrostatic interactions give rise to short-range and long-range effects. The presence of electrostatic interactions introduces the Debye length  $\kappa$ , or the characteristic length over which a charge is screened in solution, as a length scale for the polymer chain. The short-range electrostatic repulsion between charged segments separated by a distance smaller than the Debye length along the polymer backbone leads to stronger orientational correlations between chain segments and, consequently, an increase in persistence length. The long-range electrostatic repulsion between charged segments located far apart along the chain manifests as an excluded volume effect and results in an effective width greater than the bare width.

Over the past few decades, double-stranded DNA has been studied extensively at the single-molecule level as a model polymer. The ionic effects on the conformation and properties of DNA has garnered much attention, given the biological significance of DNA and highly varied ionic conditions in the intracellular environment. Furthermore, salt conditions can significantly impact the behavior of DNA in nanotechnology applications, such as nanopore sensing, <sup>8,9</sup> self-assembly <sup>10,11</sup> and biochips. <sup>12</sup> The elasticity of DNA as a function of ionic strength and in the presence of multivalent ions has been investigated, with comparisons made to theoretical predictions

of persistence length.<sup>13,14</sup> The ionic effects on the conformation and dynamics of DNA in confined geometries has also been studied, and the excluded volume effect that arises from long-range electrostatic interactions was determined to be the primary determinant of ionic strength variation of nanoconfined DNA properties.<sup>15–17</sup>

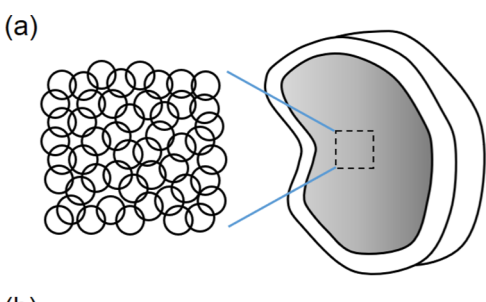
Our group has proposed the kinetoplast, a network of thousands of catenated circular DNA, as a model system for the study of two-dimensional (2D) polymers. <sup>18</sup> A kinetoplast from the trypanosomatid Crithidia fasciculata has roughly 5000 minicircles (~2.5 kbp) and 25 maxicircles (~40 kbp), with each minicircle topologically linked to three other minicircles on average and the maxicircles threaded through the minicircle network.<sup>19</sup> Fluorescent imaging reveals that kinetoplasts have a structure of an elongated wrinkled hemisphere and the 2D projection of a kinetoplast in a plane can be characterized by a major and minor axis (Figure 1). Although the repeat units of minicircles are not covalently bonded in the network, each minicircle has a fully stretched contour of approximately 5 Kuhn lengths and can be treated as an effective bond in a coarse-grained model of a 2D polymer. The kinetoplast is among the most complex mitochondrial genomes found in nature, and its unique structure has been a topic of interest in the field of cell biology, 20-22 but it has yet to be explored from a polymer physics perspective.

Recently, we probed the elasticity of kinetoplasts by studying the deformation behavior in planar elongational fields.<sup>23</sup> Inspired by the studies of ionic conditions on the properties

Received: July 22, 2020
Revised: September 16, 2020
Published: October 1, 2020







major axis
major axis

**Figure 1.** (a) Schematic of a kinetoplast resembling a cup-shaped structure with a chain mail-like network. (b) Fluorescent image of a single kinetoplast in a 2  $\mu$ m channel, with its conformation described by a major and minor axis.

of linear DNA polymers, we seek to understand the ionic effects on the equilibrium conformations of kinetoplasts as 2D polymers. In this work, we observe the conformational response of kinetoplasts to change in ionic strength. We find that the size of the kinetoplast increases isometrically with decreasing ionic strength, while there is no observed effect on the shape of the kinetoplast over the range of ionic strengths considered. The change in kinetoplast size with ionic strength is compared to a scaling argument based on a generalized Flory approach for a 2D polymer represented as monomers on an open lattice.

## 2. METHODS

**2.1. Experimental Procedure.** In this study, experiments were conducted in 2  $\mu$ m tall, 100  $\mu$ m wide, and ~1 cm long straight channels, constructed in poly(dimethylsiloxane) (PDMS, Sylgard 184, Dow Corning) using soft lithography on a silicon master template (SU8-2 photoresist). The channels were rinsed with and sonicated for 10 min in ethanol, then soaked overnight in Tris—boric acid—EDTA (TBE, AccuGENE) solution to eliminate permeation-driven flow. After being rinsed quickly with water and dried with argon, the PDMS channels were applied to clean glass cover slides (rinsed with ethanol, soaked in 1 M NaOH for at least 1 h, rinsed in water). The experimental buffer contained 4 vol %  $\beta$ -mercaptoethanol (BME, Calbiochem) and 0.1% 10 kDa poly(vinylpyrrolidone) (PVP, Polysciences) in the TBE solution. We added BME to the experimental buffer as an oxygen scavenger to minimize photodamage of the DNA, and PVP to dynamically coat the walls of the channel

and minimize electroosmotic flow. The ionic strength was varied using incremental dilutions of  $10\times$  TBE buffer (0.89 M Tris—borate, 0.02 M EDTA, pH 8.3) and ranged from 5 to 200 mM (0.02× TBE to 5× TBE). Kinetoplast DNA from *Crithidia fasciculata* (TopoGEN) was stained with fluorescent dye YOYO-1 at a base pair to dye ratio of 8:1. The stained DNA solution was stored at 4C for at least 12 h before use and diluted in an experimental buffer to a concentration of 0.1  $\mu$ g/mL immediately before experiments.

A typical experiment involved applying an electric field to electrophoretically drive kinetoplasts into the channel, waiting for 1 min to allow for equilibration, then observing the kinetoplasts for 1000 frames at a framerate of 22 frames per second. The channel height of 2  $\mu$ m, which is comparable to the ~3  $\mu$ m thickness of kinetoplasts, <sup>18</sup> weakly confined the kinetoplasts and served to orient each kinetoplast in the same observation plane perpendicular to the smallest dimension of the channel. The kinetoplasts were illuminated with a filtered light-emitting diode (Thorlabs M490L4). The filter set used was XF 100-3, which consists of an exciter filter 470AF50 (central wavelength 470 nm, bandwidth 50 nm), dichroic filter 500DRLP, and emission filter 545AF75 (central wavelength 545 nm, bandwidth 75 nm). We used an inverted Zeiss Axiovert microscope with a 63× 1.4 NA oil-immersed objective to visualize the kinetoplasts, and images were recorded by a Photometrics Prime 95B sCMOS camera. For each ionic strength, an ensemble of 30-90 kinetoplasts was observed. See the Supporting Information for details on image processing.

**2.2. Calculation of Ionic Strength.** The ionic strength is defined by  $I=1/2\sum c_i z_i^2$ , where  $c_i$  is the molar concentration and  $z_i$  is the valence of the ith ion. The ionic strength of each buffer condition was calculated by iteratively solving the system chemical equilibria for the buffer constituents. The pKa values used are for Tris base (8.06), boric acid (9.24), and EDTA (1.99, 2.67, 6.26, 10.26). We also considered BME as a weak acid in our system (pKa = 9.6). The effective concentration of the monovalent ion species was calculated by the Henderson–Hasselbalch equation. Additionally, to account for the nonideality of ions, the pKa values were corrected by calculating the activity coefficients using the Davies equation. The calculated ionic strengths (Table 1) compare well to values reported in the literature. The specific content is the strength of the literature.

**2.3.** Calculation of Persistence Length and Effective Width. For a given ionic strength I, we calculated the persistence length of DNA p using the empirical formula proposed by Dobrynin<sup>27</sup>

$$p \approx 46.1 + \frac{1.9195 \text{ M}}{\sqrt{I}} \text{nm} \tag{1}$$

To estimate the effective width w, we used the theory developed by Stigter based on mapping the second virial coefficients between pairs of charged cylinders and neutral cylinders<sup>28</sup>

$$w = \kappa^{-1} \left( 0.7704 + \log \left( \frac{\nu_{\text{eff}}^2}{2\epsilon \epsilon_0 \kappa k_{\text{B}} T} \right) \right)$$
 (2)

where

$$\kappa = \left(\frac{2N_{\rm A}e^2I}{\epsilon\epsilon_0 k_{\rm B}T}\right)^{1/2} \tag{3}$$

Table 1. Details of Calculated Parameters and Measured Values at the Different Experimental Conditions

buffer	I(M)	p (nm)	w (nm)	$\kappa  (nm^{-1})$	major axis length $L_{ m M}$ ( $\mu$ m)	minor axis length $L_{\mathrm{m}}$ ( $\mu$ m)	anisotropy $L_{\rm m}/L_{\rm M}$
$0.02 \times TBE$	$4.74 \times 10^{-3}$	74.0	22.8	0.226	$7.8 \pm 0.2$	$6.7 \pm 0.2$	$0.86 \pm 0.02$
$0.1 \times TBE$	$1.32 \times 10^{-2}$	62.8	13.6	0.378	$6.7 \pm 0.2$	$5.6 \pm 0.2$	$0.84 \pm 0.02$
$0.5 \times TBE$	$3.23 \times 10^{-2}$	56.8	9.0	0.591	$5.7 \pm 0.2$	$4.9 \pm 0.1$	$0.88 \pm 0.01$
2× TBE	$8.49 \times 10^{-2}$	52.7	6.0	0.958	$4.5 \pm 0.2$	$3.9 \pm 0.2$	$0.88 \pm 0.01$
5× TBE	$1.92 \times 10^{-1}$	50.5	4.5	1.44	$4.5 \pm 0.1$	$4.0 \pm 0.1$	$0.89 \pm 0.01$

<sup>&</sup>lt;sup>a</sup>Error bars represent 95% confidence interval.

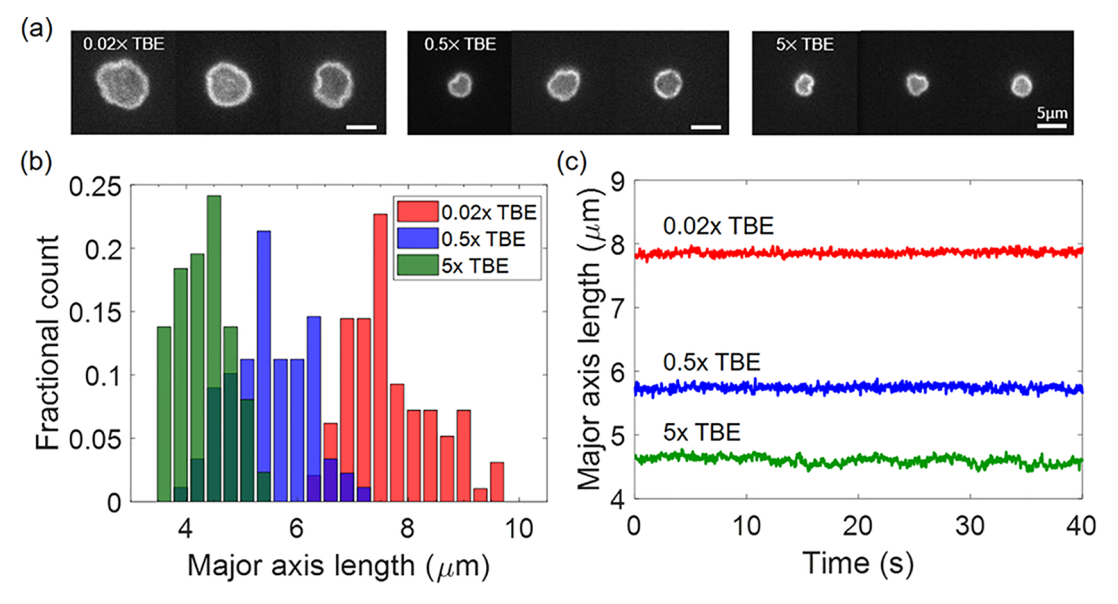


**Figure 2.** (a) Images of different kinetoplasts in  $0.02 \times \text{TBE}$ ,  $0.5 \times \text{TBE}$ , and  $5 \times \text{TBE}$ . Scale bar represents 5  $\mu$ m. (b) Histograms of major axis lengths at  $0.02 \times \text{TBE}$ ,  $0.5 \times \text{TBE}$ , and  $5 \times \text{TBE}$ . While there is some overlap in sizes between ensembles, the trend clearly shows that the average size increases at lower ionic strengths. (c) Representative traces of major axis length over time for kinetoplasts in  $0.02 \times \text{TBE}$ ,  $0.5 \times \text{TBE}$ , and  $5 \times \text{TBE}$ . The kinetoplast size fluctuates over time, but such fluctuations are small relative to the mean kinetoplast size.

is the inverse Debye length,  $\nu_{\rm eff}$  is the linear charge density,  $\epsilon$  is the dielectric constant of the medium,  $\epsilon_0$  is the permittivity of free space,  $N_{\rm A}$  is Avogadro's number, e is the elementary charge, and  $k_{\rm BT}$  is the thermal energy. The linear charge density  $\nu_{\rm eff}$  is determined as the charge density in a Debye–Huckel model that properly reproduces the far-field potential curve generated by the Guoy–Chapman model. We obtained values for  $\nu_{\rm eff}$  by interpolating between values for DNA reported by Stigter, <sup>29</sup> using an empirical formula presented by Zhang et al. <sup>30</sup>  $\nu_{\rm eff}$  = exp( $a_1$  +  $a_2$ I<sup>2/5</sup>), where  $a_1$  = 0.238 and  $a_2$  = 3.98 are fitted parameters. The persistence length, effective width, and inverse Debye length of DNA calculated for each ionic strength are reported in Table

**2.4. Size and Shape Measurements.** Assuming even distribution of the dye molecules along the backbone of the kinetoplast DNA, the fluorescence intensity of a pixel is proportional to the mass of DNA in the pixel. For each frame, we calculated the total fluorescence intensity  $F_0$ , center-of-mass vector  $\mathbf{r}_{\rm cm}(t)$ , and radius of gyration tensor  $\mathbf{G}(t)$  of the kinetoplast

$$F_0(t) = \sum_{\mathbf{m},\mathbf{n}} F_{\mathbf{m}\mathbf{n}}(t) \tag{4}$$

$$\mathbf{r}_{\text{cm},i}(t) = \frac{1}{F_0(t)} \sum_{\text{m,n}} \mathbf{r}_{\text{mn},i}(t) F_{\text{mn}}(t)$$
 (5)

$$G_{ij}(t) = \frac{1}{F_0(t)} \sum_{\mathbf{m},\mathbf{n}} (\mathbf{r}_{\mathbf{mn},i}(t) - \mathbf{r}_{\mathbf{cm},i}(t))$$

$$(\mathbf{r}_{\mathrm{mn},j}(t) - \mathbf{r}_{\mathrm{cm},j}(t))F_{\mathrm{mn}}(t) \tag{6}$$

where  $F_{\rm mn}$  is the fluorescence intensity of the pixel (m, n) and i,j represent the x,y directions in the observation plane. The radius of gyration tensor G(t) captures information about the instantaneous shape and size of the kinetoplast. The 2D projection of a kinetoplast can be described as an ellipse, and the lengths of the major and minor principal axes are given by

$$L_{\rm M} = 4\sqrt{\lambda_{\rm l}} \tag{7}$$

$$L_{\rm m} = 4\sqrt{\lambda_2} \tag{8}$$

respectively, where  $\lambda_1$  and  $\lambda_2$  ( $\lambda_1 \ge \lambda_2$ ) are the eigenvalues of **G**. The anisotropy of the kinetoplast was determined as the ratio of the minor

axis length to the major axis length. For each kinetoplast, the measurements of major axis length, minor axis length, and anisotropy were averaged over 1000 frames.

Since a population of kinetoplasts consists of kinetoplasts that are isolated at various stages of the replication cycle, <sup>20–22</sup> we observe a range of kinetoplast sizes at equilibrium. <sup>23</sup> To prevent the ensemble average size from being biased by the larger kinetoplasts observed, we omitted kinetoplasts with a major axis length two standard deviations above the mean from each ensemble. See Table 1 for the ensemble average size measurements at the different ionic strengths.

To characterize the shapes of the kinetoplasts, we used an edge detection algorithm detailed in a previous publication. Since the edge of a kinetoplast is much brighter than the rest of the molecule, we could determine the outline of the kinetoplast by identifying the connected regions of maximum intensity in each image. This was achieved by applying the extended-maxima transform, which is the regional maxima of the H-maxima transform, where the threshold intensity value of H was iteratively increased until the identified region maxima formed a contiguous ring. The polar coordinates of the outline of the ring, described by 72 points separated by  $S^{\circ}$  each, were then taken to be the edge of the kinetoplast.

A quantitative method for analyzing the shapes of kinetoplasts is principal component analysis (PCA).<sup>32</sup> The outline of each kinetoplast represents a point in a 72-dimensional vector space. Before performing PCA, we first rotated the edge coordinates of each kinetoplast such that the major axis was aligned with the horizontal axis. We constructed an n by 72 matrix S, where n is the number of kinetoplasts in the ensemble, containing the edge coordinates of the kinetoplasts. To avoid potential bias introduced by size effects, the edge coordinates for each kinetoplast were standardized by subtracting the mean and dividing by the standard deviation.<sup>32</sup> We computed the covariance matrix C of the matrix S, given by

$$C_{i,j} = \frac{1}{n-1} \sum_{k=1}^{n} (S_{ki} - \overline{S}_i)(S_{kj} - \overline{S}_j)$$
(9)

The eigenvectors of the covariance matrix *C* represent the principal components (PCs) and were ordered by the magnitude of the corresponding eigenvalues from largest to smallest, such that the first principal component explains the largest variance in the data set. To visualize the PC shapes, we plotted the eigenvectors using a radius equal to the average magnitude of the outline coordinates. The

coordinates of each kinetoplast outline in the PC-space were obtained from the dot product of the standardized edge coordinates and principal components.

#### 3. RESULTS AND DISCUSSION

**3.1. Kinetoplast Size.** Figure 2 shows the effects of ionic strength on the equilibrium size of kinetoplasts. Since the mean anisotropy of kinetoplasts does not vary much with ionic strength (Table 1), the choice of major or minor axis length as the measure of kinetoplast size is arbitrary. An increase in ionic strength leads to stronger electrostatic screening, which results in a decrease in kinetoplast size. Despite some overlap in the distributions of major axis lengths for kinetoplasts in 0.02× TBE, 0.5× TBE, and 5× TBE, there is a distinct shift in size as the ionic strength is increased (see the Supporting Information for distributions for all ionic strengths). We note that the fluctuations in size for a kinetoplast at a given ionic strength are small relative to the difference in size attributable to the ionic effects. In Figure 3, we plot the change in major axis

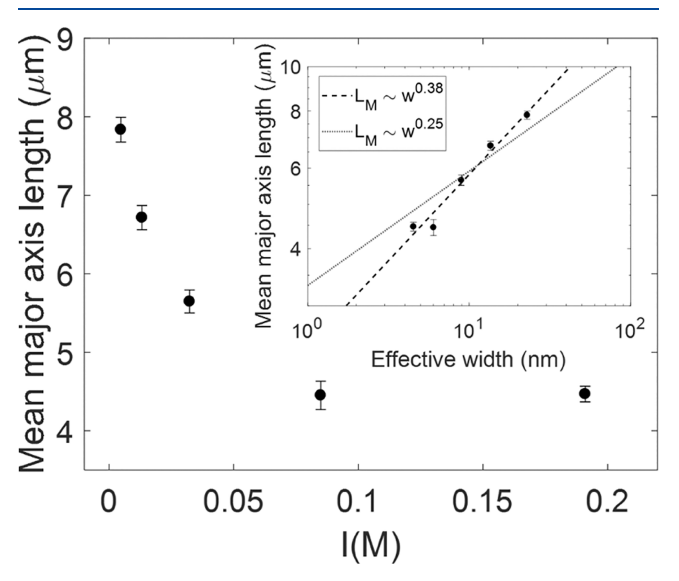


**Figure 3.** Mean major axis length as a function of ionic strength. Inset: Log-log plot of mean major axis length as a function of effective width. The dashed line represents a fit to  $L_{\rm M}=\alpha_1 w^{\beta}$ , yielding  $\beta=0.38\pm0.11$ . The dotted line represents a fit to  $L_{\rm M}=\alpha_2 w^{0.25}$ , shown for the purposes of comparison. Error bars represent 95% confidence interval.

length with ionic strength. The kinetoplast size varies almost twofold over the range of ionic strengths used in experiments. We observe a plateau in kinetoplast size at the higher ionic strengths investigated, due to the effective width of DNA leveling off at high ionic strengths. Given that the variation in effective width is much stronger than the variation in persistence length over the range of ionic strengths considered (Table 1), it can be inferred that the change in kinetoplast size with ionic strength is driven by the long-range electrostatic repulsion that gives rise to a change in effective width, as was similarly observed with nanoconfined linear DNA in a comparable ionic strength range. <sup>15,16</sup>

To understand the quantitative change in kinetoplast size with ionic strength, we develop a scaling argument based on a Flory type approach for a 2D polymer confined in a slit geometry. Given the self-avoidance of DNA, we believe the kinetoplasts to be in the flat phase. <sup>33–35</sup> Hence, we obtain the

generalized Flory exponent  $\nu=1$  and find two-body interactions to be mean-field relevant for our system. <sup>36,37</sup>

We recall that the kinetoplast is a planar network of catenated circular DNA. To build a tractable scaling theory, we propose a simplified representation of the kinetoplast as a 2D network of DNA polymer chains connected at fixed vertices (Figure 4), akin to models developed for the erythrocyte

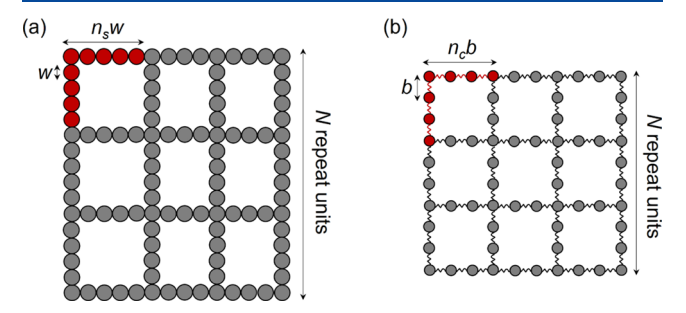


**Figure 4.** (a) Open lattice representation of a 2D polymer with spherical monomers of diameter w, and  $n_s$  monomers between fixed vertices. (b) Coarse-grained representation of a 2D polymer with cylindrical monomers of Kuhn length b, diameter w, and  $n_c$  monomers between fixed vertices. The repeat units are colored in red.

cytoskeleton.<sup>38</sup> We coarse-grain the complex geometry of the kinetoplast to a series of linear polymer chains of width w, with  $n_{\rm c}$  segments of Kuhn length b connected at fixed vertices. For simplicity, we consider an open square lattice. Other open lattice geometries would simply introduce a different dimensionless numerical prefactor in the calculation, which would be neglected in a scaling argument.

The conformation of the 2D polymer system is determined by a balance between the elastic free energy and excluded volume interaction energy.<sup>39</sup> The Flory free energy for a Ddimensional polymer confined in a slit is given by

$$\frac{F}{k_{\rm B}T} \sim \frac{R_{\parallel}^2}{N^{2-D}b^2} + \frac{\nu N^{2D}}{hR_{\parallel}^2} \tag{10}$$

where  $R_{\parallel}$  is the size of the confined polymer, N is the number of monomers in a given direction, b is the Kuhn length, v is the mean-field approximated excluded volume parameter, and h is the slit height. For D=2, minimization of the free energy leads to

$$R_{\parallel} \sim \frac{v^{1/4} b^{1/2} N}{h^{1/4}} \tag{11}$$

The excluded volume parameter  $\nu$  for our 2D polymer model is  $\nu \sim b^2 w$  (see the Supporting Information for derivation); hence, the equilibrium size of the polymer is

$$R_{\parallel} \sim \frac{w^{1/4}L}{h^{1/4}}$$
 (12)

where L=Nb is the linear size of the polymer when flattened and fully extended. The scaling result predicts no dependence on the Kuhn length and, consequently, the persistence length, suggesting from a theoretical perspective that the change in effective width is the primary determinant of the observed ionic effects on kinetoplast size. This is in contrast to the scaling law for a linear polymer in a slit  $^{16}$   $R_{\parallel} \sim (bw)^{1/4} \, L^{3/4} h^{-1/4}$ . See the Supporting Information for the derivation of the scaling argument using a blob model.

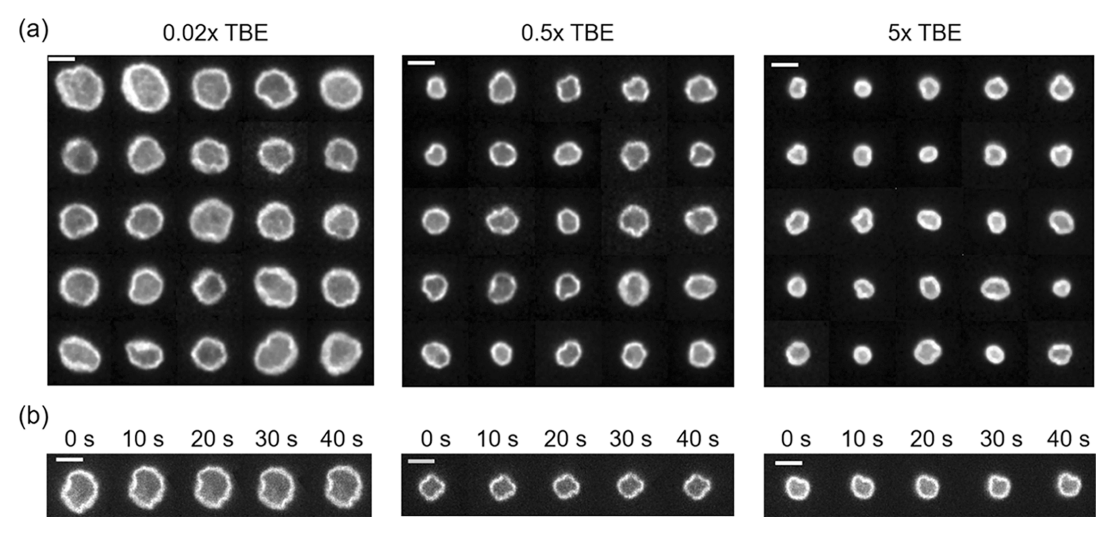


**Figure 5.** (a) Montage of images of different kinetoplasts in  $0.02 \times \text{TBE}$ ,  $0.5 \times \text{TBE}$ , and  $5 \times \text{TBE}$ . (b) Snapshots of three select kinetoplasts in  $0.02 \times \text{TBE}$ ,  $0.5 \times \text{TBE}$ , and  $5 \times \text{TBE}$  at different time points as labeled. The images are rotated to maintain the kinetoplast orientation with time to highlight the fact that their overall shape does not change appreciably. Scale bars represent 5  $\mu$ m.

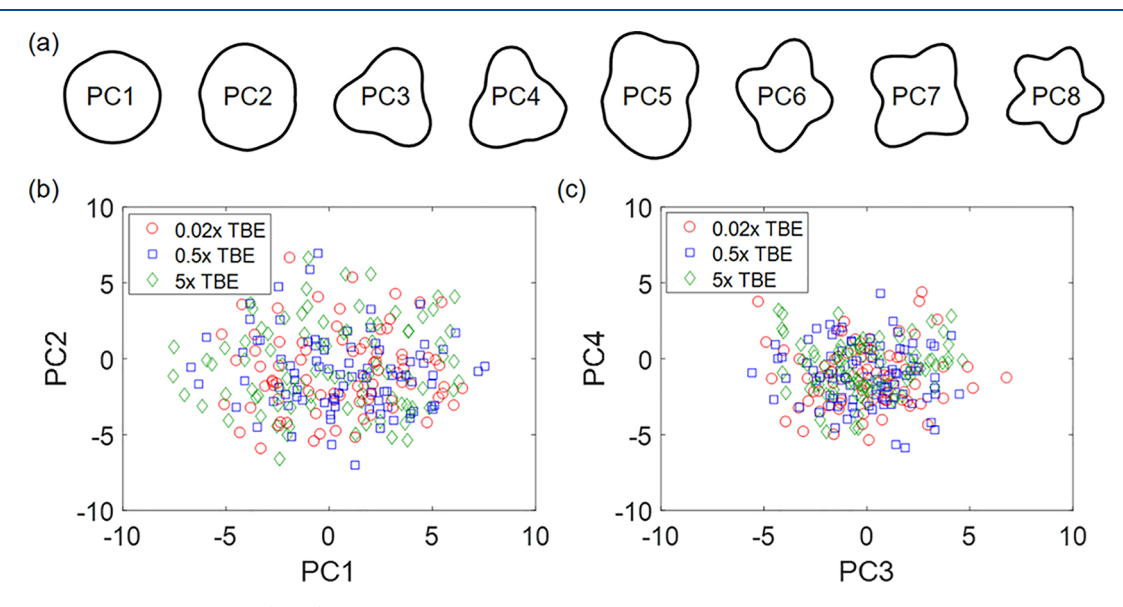


**Figure 6.** Principal component analysis (PCA) of kinetoplast edge shapes for a combined ensemble of kinetoplasts in 0.02× TBE, 0.5× TBE, and 5× TBE. (a) Images of the first eight principal components (PCs). Scatter plots of the (b) first and second PC amplitudes, and (c) third and fourth PC amplitudes for kinetoplasts in 0.02× TBE, 0.5× TBE, and 5× TBE.

As seen from Figure 3, we obtain a stronger scaling of  $L_{\rm M} \sim w^{0.38}$  from the experimental data. We take into consideration possible factors that can account for the discrepancy. First, the scaling analysis is based on a simplified 2D polymer model and mean-field approximation of the Flory argument. In reality, the kinetoplast is a system with a complex topology that is difficult to model. Second, the ionic strengths presented are theoretically calculated and not experimentally measured. The true ionic strengths of the buffer solutions might differ, for example, due to potential residual ions present in the staining buffer that are not accounted for in our calculations.

We note that the range of salt concentrations investigated in this study is such that the salt concentrations are always much larger than the polymer charge concentration and the Debye lengths are smaller than the electrostatic blob size (see the Supporting Information). Therefore, the interactions between monomers are predominantly short-range and can be viewed as excluded volume interactions.<sup>40</sup> As the ionic strength is further decreased, the scaling argument presented begins to break down and a different analysis approach that accounts for Donnan equilibrium would be required.<sup>41</sup>

**3.2. Kinetoplast Shape.** Previous work from our group <sup>18</sup> reported visible differences in the shapes of kinetoplasts in a given population, attributed to the unique topology of the underlying network connectivity, and the differences in shape were quantitatively captured using principal component analysis (PCA). Having investigated the change in kinetoplast size with ionic strength, we now probe the ionic effects on kinetoplast shape. Figure 5a shows images of 25 different kinetoplasts in 0.02× TBE, 0.5× TBE, and 5× TBE. With our eye, we can see that each kinetoplast has a distinct shape that differentiates it from others. We point out that for all ionic strengths considered, the shape of each kinetoplast remains persistent over the observation window of 40 s (Figure 5b), a

timescale that is 2 orders of magnitude greater than the short fluctuation timescale of  $\sim \! 0.1 \ s.^{18}$ 

At a given ionic strength, a population of kinetoplasts will exhibit a distribution of shapes. The question we would like to address is whether such a distribution varies with ionic strength. One might expect that the larger sizes of kinetoplasts at lower ionic strengths would result in more uniform shapes, due to the stronger degree of confinement within the channel. We use PCA to analyze the edge coordinates of a combined ensemble of kinetoplasts in 0.02× TBE, 0.5× TBE, and 5× TBE (Figure 6). To visualize the variation in shapes across kinetoplasts at different ionic strengths, we plot the locations of each kinetoplast outline in the PC1-PC2 and PC3-PC4 space. Surprisingly, there does not appear to be a stratification of data points with respect to ionic strength, indicating that the distribution of kinetoplast shapes in a given ensemble does not vary with ionic strength. Increasing or decreasing the electrostatic screening has a dramatic effect on the kinetoplast size, but the change in size is not accompanied by an evident change in shape. This suggests that the underlying topology of the kinetoplasts remains unchanged under different ionic conditions, despite the change in the extent of confinement that accompanies the change in size. Upon further confinement, we may see a transition akin to the de Gennes to Odijk regime in linear polymers<sup>42</sup> that would yield a distinct change in kinetoplast shape. See the Supporting Information for plots in the PC5-PC6 and PC7-PC8 space and the results of PCA applied to each ensemble separately.

# 4. CONCLUSIONS

In this work, we studied the ionic effects on the equilibrium size and shape of kinetoplasts. We observed kinetoplasts at equilibrium in ionic strengths ranging from 5 to 200 mM. With an increase in ionic strength, the stronger screening of electrostatic interactions results in a decrease in kinetoplast size. The major axis length of kinetoplasts is found to scale with effective width as  $L_{\rm M} \sim w^{0.38}$ , yielding a scaling exponent larger than that predicted from a Flory type argument for a 2D polymer model. The scaling argument also predicted that the change in kinetoplast size with ionic strength in a slit is driven by the change in effective width, not persistence length. This is in contrast to the scaling theory for a linear polymer in a slit where the polymer size scales with both width and persistence length in the same manner. While ionic strength has a dramatic impact on kinetoplast size, it does not noticeably affect the distribution of kinetoplast shapes which appear over all conditions as a wrinkled hemisphere. In the future, it would be interesting to examine if these wrinkles persist under more extreme microfluidic confinement.

Our study provides insight into the ionic effects on the equilibrium conformation of a catenated DNA network. The unique catenated structure of kinetoplasts gives them flexibility in comparison to more conventional 2D materials such as graphene. While crystalline 2D materials have unique electronic properties, 2D soft materials are desirable for applications in stretchable electronics, and as versatile membranes for optoelectronics and chemical separation. From an applications standpoint, understanding the effect of biological buffer conditions can help guide engineering practices to design implantable electronics or cell therapeutics. Moving forward, we hope that this work will motivate future single-molecule studies using kinetoplasts to help elucidate the biophysical problems of 2D polymers.

#### ASSOCIATED CONTENT

# Supporting Information

The Supporting Information is available free of charge at https://pubs.acs.org/doi/10.1021/acs.macromol.0c01706.

Details on image processing and principal component analysis; size distributions of kinetoplasts; derivation of excluded volume parameter for 2D polymer model and scaling argument using the blob model (PDF)

#### AUTHOR INFORMATION

# **Corresponding Author**

Patrick S. Doyle — Department of Chemical Engineering, Massachusetts Institute of Technology, Cambridge, Massachusetts 02139, United States; ⊚ orcid.org/0000-0003-2147-9172; Email: pdoyle@mit.edu

#### **Authors**

Beatrice W. Soh — Department of Chemical Engineering, Massachusetts Institute of Technology, Cambridge, Massachusetts 02139, United States; orcid.org/0000-0001-8399-5995

Ahmed Khorshid – Department of Chemical Engineering, Massachusetts Institute of Technology, Cambridge, Massachusetts 02139, United States

Dana Al Sulaiman – Department of Chemical Engineering, Massachusetts Institute of Technology, Cambridge, Massachusetts 02139, United States

Complete contact information is available at: https://pubs.acs.org/10.1021/acs.macromol.0c01706

#### **Author Contributions**

<sup>T</sup>B.W.S. and A.K. contributed equally to this work.

#### Notes

The authors declare no competing financial interest.

#### ACKNOWLEDGMENTS

This work was supported by the National Science Foundation (NSF) grant CBET-1936696. B.W.S. is funded by the Agency for Science, Technology and Research (A\*STAR), Singapore. D.A.S. acknowledges generous funding from the KACST-MIT Ibn Khaldun Fellowship. We acknowledge Alexander Klotz for thoughtful discussions.

# REFERENCES

- (1) Jiang, H.; Taranekar, P.; Reynolds, J. R.; Schanze, K. S. Conjugated Polyelectrolytes: Synthesis, Photophysics, and Applications. *Angew. Chem., Int. Ed.* **2009**, *48*, 4300–4316.
- (2) Zhao, Q.; An, Q. F.; Ji, Y.; Qian, J.; Gao, C. Polyelectrolyte Complex Membranes for Pervaporation, Nanofiltration and Fuel Cell Applications. *J. Membr. Sci.* **2011**, *379*, 19–45.
- (3) Mecerreyes, D. Polymeric Ionic Liquids: Broadening the Properties and Applications of Polyelectrolytes. *Prog. Polym. Sci.* **2011**, *36*, 1629–1648.
- (4) von Hippel, P. H.; Schleich, T. Ion Effects on the Solution Structure of Biological Macromolecules. *Acc. Chem. Res.* **1969**, *2*, 257–265.
- (5) Odijk, T. Polyelectrolytes Near the Rod Limit. J. Polym. Sci., Polym. Phys. Ed. 1977, 15, 477-483.
- (6) Skolnick, J.; Fixman, M. Electrostatic Persistence Length of a Wormlike Polyelectrolyte. *Macromolecules* 1977, 10, 944–948.
- (7) Odijk, T.; Houwaart, A. C. On the Theory of the Excluded-Volume Effect of a Polyelectrolyte in a 1-1 Electrolyte Solution. *J. Polym. Sci., Polym. Phys. Ed.* **1978**, *16*, 627–639.

- (8) Smeets, R. M. M.; Keyser, U. F.; Krapf, D.; Wu, M. Y.; Dekker, N. H.; Dekker, C. Salt Dependence of Ion Transport and DNA Translocation Through Solid-State Nanopores. *Nano Lett.* **2006**, *6*, 89–95.
- (9) Wanunu, M.; Morrison, W.; Rabin, Y.; Grosberg, A. Y.; Meller, A. Electrostatic Focusing of Unlabelled DNA into Nanoscale Pores Using a Salt Gradient. *Nat. Nanotechnol.* **2010**, *5*, 160–165.
- (10) Woo, S.; Rothemund, P. W. K. Self-Assembly of Two-Dimensional DNA Origami Lattices Using Cation-Controlled Surface Diffusion. *Nat. Commun.* **2014**, *5*, No. 4889.
- (11) Kim, H.; Surwade, S. P.; Powell, A.; O'Donnell, C.; Liu, H. Stability of DNA Origami Nanostructure Under Diverse Chemical Environments. *Chem. Mater.* **2014**, *26*, 5265–5273.
- (12) Bracha, D.; Karzbrun, E.; Shemer, G.; Pincus, P. A.; Bar-Ziv, R. H. Entropy-Driven Collective Interactions in DNA Brushes on a Biochip. *Proc. Natl. Acad. Sci. U.S.A.* **2013**, *110*, 4534–4538.
- (13) Baumann, C. G.; Smith, S. B.; Bloomfield, V. A.; Bustamante, C. Ionic Effects on the Elasticity of Single DNA Molecules. *Proc. Natl. Acad. Sci. U.S.A.* 1997, 94, 6185–6190.
- (14) Guilbaud, S.; Salomé, L.; Destainville, N.; Manghi, M.; Tardin, C. Dependence of DNA Persistence Length on Ionic Strength and Ion Type. *Phys. Rev. Lett.* **2019**, *122*, No. 028102.
- (15) Reisner, W.; Beech, J. P.; Larsen, N. B.; Flyvbjerg, H.; Kristensen, A.; Tegenfeldt, J. O. Nanoconfinement-Enhanced Conformational Response of Single DNA Molecules to Changes in Ionic Environment. *Phys. Rev. Lett.* **2007**, *99*, No. 058302.
- (16) Hsieh, C. C.; Balducci, A.; Doyle, P. S. Ionic Effects on the Equilibrium Dynamics of DNA Confined in Nanoslits. *Nano Lett.* **2008**, *8*, 1683–1688.
- (17) Lin, P. K.; Hsieh, C. C.; Chen, Y. L.; Chou, C. F. Effects of Topology and Ionic Strength on Double-Stranded DNA Confined in Nanoslits. *Macromolecules* **2012**, *45*, 2920–2927.
- (18) Klotz, A. R.; Soh, B. W.; Doyle, P. S. Equilibrium Structure and Deformation Response of 2D Kinetoplast Sheets. *Proc. Natl. Acad. Sci. U.S.A.* **2020**, *117*, 121–127.
- (19) Englund, P. T. The Replication of Kinetoplast DNA Networks in *Crithidia Fasciculata*. Cell 1978, 14, 157–168.
- (20) Shapiro, T. A.; Englund, P. T. The Structure and Replication of Kinetoplast DNA. *Annu. Rev. Microbiol.* **1995**, *49*, 117–143.
- (21) Liu, B.; Liu, Y.; Motyka, S. A.; Agbo, E. E. C.; Englund, P. T. Fellowship of the Rings: The Replication of Kinetoplast DNA. *Trends Parasitol.* **2005**, *21*, 363–369.
- (22) Jensen, R. E.; Englund, P. T. Network News: The Replication of Kinetoplast DNA. *Annu. Rev. Microbiol.* **2012**, *66*, 473–491.
- (23) Soh, B. W.; Doyle, P. S. Deformation Response of Catenated DNA Networks in a Planar Elongational Field. ACS Macro Lett. 2020, 9, 944–949.
- (24) Randall, G. C.; Doyle, P. S. Permeation-Driven Flow in Poly(dimethylsiloxane) Microfluidic Devices. *Proc. Natl. Acad. Sci. U.S.A.* **2005**, *102*, 10813–10818.
- (25) Danehy, J. P.; Noel, C. J. The Relative Nucleophilic Character of Several Mercaptans Toward Ethylene Oxide. *J. Am. Chem. Soc* **1960**, 82, 2511–2515.
- (26) Butler, J. N. Ionic Equilibrium: Solubility and pH Calculations; Wiley, 1998.
- (27) Dobrynin, A. V. Effect of Counterion Condensation on Rigidity of Semiflexible Polyelectrolytes. *Macromolecules* **2006**, 39, 9519–9527.
- (28) Stigter, D. Interactions of Highly Charged Colloidal Cylinders with Applications to Double-Stranded DNA. *Biopolymers* 1977, 16, 1435–1448.
- (29) Stigter, D.; Dill, K. A. Theory for Second Virial Coefficients of Short DNA. J. Phys. Chem. A 1993, 97, 12995–12997.
- (30) Zhang, Y.; Zhou, H.; Ou-Yang, Z. C. Stretching Single-Stranded DNA: Interplay of Electrostatic, Base-Pairing, and Base-Pair Stacking Interactions. *Biophys. J.* **2001**, *81*, 1133–1143.
- (31) Hsieh, C. C.; Balducci, A. G.; Doyle, P. S. An Experimental Study of DNA Rotational Relaxation Time in Nanoslits. *Macromolecules* **2007**, *40*, 5196–5205.

- (32) Pincus, Z.; Theriot, J. A. Comparison of Quantitative Methods for Cell-Shape Analysis. *J. Microsc.* **2007**, 227, 140–156.
- (33) Plischke, M.; Boal, D. Absence of a Crumpling Transition in Strongly Self-Avoiding Tethered Membranes. *Phys. Rev. A* **1988**, 38, 4943—4945
- (34) Abraham, F. F.; Rudge, W. E.; Plischke, M. Molecular Dynamics of Tethered Membranes. *Phys. Rev. Lett.* **1989**, *62*, 1757–1759.
- (35) Kantor, Y.; Kremer, K. Excluded-Volume Interactions in Tethered Membranes. *Phys. Rev. E* **1993**, *48*, 2490–2497.
- (36) Cates, M. E. Statics and Dynamics of Polymeric Fractals. *Phys. Rev. Lett.* **1984**, *53*, 926–929.
- (37) Schlüter, A. D.; Payamyar, P.; Öttinger, H. C. How the World Changes By Going from One- to Two-Dimensional Polymers in Solution. *Macromol. Rapid Commun.* **2016**, 37, 1638–1650.
- (38) Boal, D. Mechanics of the Cell; Cambridge University Press: Cambridge, 2012.
- (39) Rubinstein, M.; Colby, R. H. Polymer Physics; Oxford University Press, 2003.
- (40) Dobrynin, A. V.; Rubinstein, M. Theory of Polyelectrolytes in Solutions and at Surfaces. *Prog. Polym. Sci.* **2005**, *30*, 1047–1118.
- (41) Rubinstein, M.; Colby, R. H.; Dobrynin, A. V.; Joanny, J. F. Elastic Modulus and Equilibrium Swelling of Polyelectrolyte Gels. *Macromolecules* **1996**, 29, 398–406.
- (42) Reisner, W.; Morton, K. J.; Riehn, R.; Wang, Y. M.; Yu, Z.; Rosen, M.; Sturm, J. C.; Chou, S. Y.; Frey, E.; Austin, R. H. Statics and Dynamics of Single DNA Molecules Confined in Nanochannels. *Phys. Rev. Lett.* **2005**, *94*, No. 196101.
- (43) Akinwande, D.; Brennan, C. J.; Bunch, J. S.; Egberts, P.; Felts, J. R.; Gao, H.; Huang, R.; Kim, J. S.; Li, T.; Li, Y.; Liechti, K. M.; Lu, N.; Park, H. S.; Reed, E. J.; Wang, P.; Yakobson, B. I.; Zhang, T.; Zhang, Y. W.; Zhou, Y.; Zhu, Y. A Review on Mechanics and Mechanical Properties of 2D Materials Graphene and Beyond. *Extreme Mech. Lett.* 2017, 13, 42–77.
- (44) Zhuang, X.; Mai, Y.; Wu, D.; Zhang, F.; Feng, X. Two-Dimensional Soft Nanomaterials: A Fascinating World of Materials. *Adv. Mater.* **2015**, *27*, 403–427.
- (45) Ernst, A. U.; Wang, L.-H.; Ma, M. Interconnected Toroidal Hydrogels for Islet Encapsulation. *Adv. Healthcare Mater.* **2019**, 8, No. 1900423.